

RESEARCH ARTICLE

10.1002/2016JA022816

Emission of magnetosound from MHD-unstable shear flow boundaries

H. Turkakin¹, R. Rankin¹, and I. R. Mann¹¹Department of Physics, University of Alberta, Edmonton, Alberta, Canada

Key Points:

- Emission of magnetosonic waves due to KHI is possible along various MHD shear flow boundaries in solar-terrestrial environment
- The efficiency of magnetosonic wave emission due to KHI increases with increasing magnetic tension along these shear flow boundaries
- MHD wave emission due to KHI may be a mean of energy transportation between various regions in the solar-terrestrial environment

Supporting Information:

- Supporting Information S1

Correspondence to:

H. Turkakin,
turkakin@ualberta.ca

Citation:

Turkakin, H., R. Rankin, and I. R. Mann (2016), Emission of magnetosound from MHD-unstable shear flow boundaries, *J. Geophys. Res. Space Physics*, 121, 8740–8754, doi:10.1002/2016JA022816.

Received 16 APR 2016

Accepted 7 SEP 2016

Accepted article online 12 SEP 2016

Published online 28 SEP 2016

Abstract The emission of propagating MHD waves from the boundaries of flow channels that are unstable to the Kelvin-Helmholtz Instability (KHI) in magnetized plasma is investigated. The KHI and MHD wave emission are found to be two competing processes. It is shown that the fastest growing modes of the KHI surface waves do not coincide with efficient wave energy transport away from a velocity shear boundary. MHD wave emission is found to be inefficient when growth rates of KHI surface waves are maximum, which corresponds to the situation where the ambient magnetic field is perpendicular to the flow channel velocity vector. The efficiency of wave emission increases with increasing magnetic field tension, which in Earth's magnetosphere likely dominates along the nightside magnetopause tailward of the terminator, and within earthward Bursty Bulk Flows (BBFs) in the inner plasma sheet. MHD wave emission may also dominate in Supra-Arcade Downflows (SADs) in the solar corona. Our results suggest that efficient emission of propagating MHD waves along BBF and SAD boundaries can potentially explain observations of deceleration and stopping of BBFs and SADs.

1. Introduction

Kelvin-Helmholtz Instability (KHI) is a type of instability that may occur along hydrodynamic and magneto-hydrodynamic (MHD) shear flow boundaries. Due to its significant effects on fluid mixing and energy and momentum transfer in between two different flowing media, the KHI has been studied extensively in both hydrodynamic [e.g., Lawrence *et al.*, 1991; Malik *et al.*, 1994; Jean and Laurent, 2000] and magnetohydrodynamic (MHD) [e.g., Walker, 1981; Miura and Pritchett, 1982; Pu and Kivelson, 1983; Taroyan and Erdélyi, 2003; Lai and Lyu, 2006] limits. The evolution of the KHI is more complex in the presence of magnetic fields and ionized media because magnetic pressure and tension forces act on the flowing plasma in a variety of ways different from the hydrodynamic case. With the inclusion of ambient magnetic fields, magnetic pressure and tension forces combined with nonmagnetic forces introduce new types of waves resulting in more complex interactions between the flow and perturbations [Taroyan and Ruderman, 2011]. If the background magnetic field is purely perpendicular to the shear flow, the KHI will occur at any flow speed value, i.e., there is no lower cutoff velocity. A component of the background magnetic field parallel to the shear flow inhibits the evolution of KHI. With a larger parallel component of the ambient magnetic field, the cutoff speed at which KHI onset occurs increases and the strength of the growth decreases [e.g., Miura and Pritchett, 1982; Pu and Kivelson, 1983; Mann *et al.*, 1999].

Studies have been performed on the characteristics of the linear [Walker, 1981; Miura and Pritchett, 1982; Pu and Kivelson, 1983; Taroyan and Erdélyi, 2002] and nonlinear [Miura, 1982; Rankin *et al.*, 1997; Lai and Lyu, 2006, 2008] evolution of MHD KHI. Several important aspects of the KHI have been discovered, such as the possibility for driving field line resonances [Southwood, 1974; Walker, 1981], causing magnetic reconnection during northward interplanetary magnetic field (IMF) [Fairfield *et al.*, 2000; Takagi *et al.*, 2006], and carrying energy and momentum across the magnetopause boundary [Hasegawa *et al.*, 2006; Taroyan and Ruderman, 2011].

Some studies have assumed a zero thickness boundary, which is appropriate if the wavelengths of the generated waves are significantly larger than the thickness of the boundary [Pu and Kivelson, 1983; Mann *et al.*, 1999; Turkakin *et al.*, 2013, 2014]. The effects of a finite boundary thickness have also been investigated in several studies [Ong and Roderick, 1972; Walker, 1981; Farrugia *et al.*, 1998; Contin *et al.*, 2003; Gratton *et al.*, 2004]. The main effect of including a finite thickness boundary is that only perturbations with sufficiently small wave numbers are unstable [Walker, 1981; Miura and Pritchett, 1982; Gratton *et al.*, 2004].

The KHI is also an important process along the interface of the heliopause, in the solar atmosphere, and in remote astrophysical objects such as accretion disks near neutron stars and black holes [Taroyan and Ruderman, 2011]. The KHI is suggested to be possible in solar plumes leading to the disruption and mixing of plumes with interplume plasma [e.g., Andries and Goossens, 2001]. The Atmospheric Imaging Assembly (AIA) on board the Solar Dynamics Observatory (SDO) and the Large Angle and Spectrometric Coronagraph Experiment (LASCO) on board the Solar and Heliospheric Observatory (SOHO) have observed occurrences of KHI in the solar corona at velocity shear boundaries, including the flanks of high-speed coronal mass ejections (CMEs) [Liu and Ofman, 2006; Foullon et al., 2011, 2013; Möstl et al., 2013], solar prominences, and high-corona streamers [Feng et al., 2013]. Liu and Ofman [2006] have reported observations of KHI and associated waves in the solar corona. Several numerical studies have also investigated the KHI along the boundaries of CMEs [Foullon et al., 2013; Möstl et al., 2013; Nykyri and Foullon, 2013], Supra-Arcade Downflows (SADs) [Cécere et al., 2014], coronal plumes [Andries and Goossens, 2001], and coronal streamers [Feng et al., 2013].

Surprisingly, the emission of propagating MHD waves from a shear flow boundary as an effect of the KHI has received little attention. The spontaneous emission of sound waves between two counterstreaming media was first suggested by Landau and Lifshitz [1987] as propagating small perturbations in a medium moving with relative supersonic velocities. Mann et al. [1999] have suggested that at sufficiently large magnetosheath flow speeds, overreflected surface modes may turn into body modes and carry energy into the magnetosphere. This situation was suggested to be a representation of emission of magnetosound from the boundary of a moving medium. Planar waves moving away from KHI vortices have been reported in a few studies in the past [Lai and Lyu, 2006, 2008]. In these studies propagating waves are attributed to nonlinear processes, and no connection between them and the linear growth of the KHI was inferred. Turkakin et al. [2014] have shown that KHI and MHD wave emission due to KHI may occur along the boundaries of Bursty Bulk Flows (BBFs) in the central plasma sheet of the Earth. These KHI emitted waves are suggested to be a possible means of carrying available energy out of BBF channel boundaries and stopping the BBFs in the near-Earth regions.

In the current study, emission of MHD waves from a shear flow boundary is shown to exist during the linear stages of the KHI evolution. The relation between the emission of propagating magnetosonic waves, the growth rates of KHI waves, and their wave numbers is clearly described. Linear MHD theory is used to compute the KHI growth rates of the MHD modes supported by a shear flow boundary with a nonzero thickness. The effects of background magnetic field directions on magnetosonic wave emission are investigated in detail. The results are used to predict the efficiency of MHD wave emission along shear flow boundaries in the magnetospheric regions of Earth—along the magnetopause and the edges of BBF channels. The possibility of MHD wave emission due to KHI along shear flow boundaries in the solar corona, such as SADs and CMEs, is also discussed.

2. Boundary Layer Model and Numerical Techniques

A 1-D simplified model of a shear flow boundary is considered consisting of two semi-infinite plasma regions separated by a boundary layer region of thickness $\Delta_x = 2h$. All zero-order quantities are assumed to vary only along x direction. Model parameters are illustrated schematically in Figure 1. In this model, the background density ρ_0 , magnetic field \mathbf{B}_0 , and plasma pressure P_0 change discontinuously across an interface of zero thickness placed at $x = -h$, while the velocity \mathbf{U}_0 varies with x over a layer of thickness Δ_x . The assumption of a step-like change in ρ_0 , B_0 , and P_0 is valid if the variations of these parameters in the real system take place over a distance δ_l much smaller than Δ_x . Additionally, the transverse wavelength λ_x must be much greater than δ_l . For perturbations where $\lambda_x \leq \delta_l$, continuous variations of ρ_0 , B_0 and P_0 need to be considered [cf. Gratton et al., 2004]. The assumptions of the model, while somewhat idealized, allow a large range of parameter space to be investigated. The background magnetic field is assumed to lie in the tangent plane of the boundary, i.e., the y - z plane. Without the loss of generality, the zero-order streaming velocity is assumed along y direction. The values of U_0 are set to constant values of $(U_{01} - U_{02})/2$ in region 1 and $-(U_{01} - U_{02})/2$ in region 2 and vary as $U_0(x) = (U_{02} - U_{01}) (3x/h - (x/h)^3) / 4$ in the transition layer region. This profile was used by Walker [1981] as it is convenient for investigating effects of magnetic shear, density variation, and the ratio of magnetic to thermal energy on the KHI.

The stability of the boundary defined above is studied with linearized ideal MHD assuming small amplitude perturbations in warm compressible homogeneous plasmas in regions 1 and 2 and the boundary layer region.

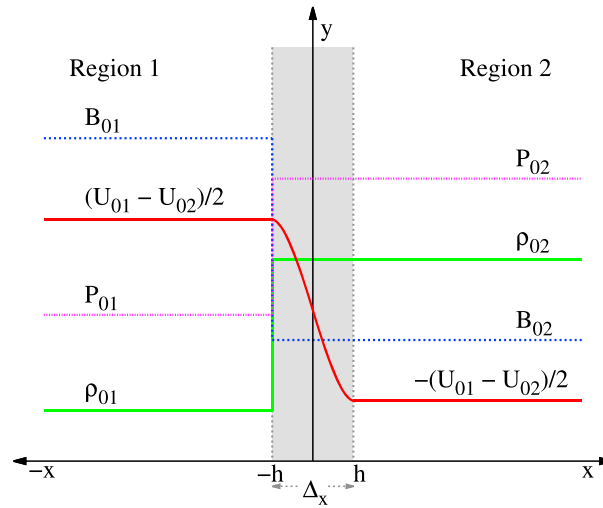


Figure 1. Schematic of the magnetospheric boundary layer model used. $\Delta_x = 2h$ is the boundary layer thickness. The background values of magnetic fields, B_{01} , B_{02} ; densities, ρ_{01} , ρ_{02} ; and plasma pressures, P_{01} , P_{02} are varied sharply at $x = -h$. Velocity, $U_0(x)$, connects two intervals of constant values $(U_{01} - U_{02})/2$ and $-(U_{01} - U_{02})/2$ with a linear function in the transition layer region such that $U_0(x) = (U_{02} - U_{01}) (3x/h - (x/h)^3) / 4$.

permeability of free space, and γ is the adiabatic index. The detailed derivation of equation (1) can be found in Walker [1981]. Equation (1) can be rearranged in a form as

$$\frac{d^2 \delta x}{dx^2} + \left(\frac{1}{\chi} \frac{d\chi}{dx} \right) \frac{d\delta x}{dx} + k_x^2 \delta x = 0. \quad (3)$$

Equation (3) is applicable to regions 1 and 2 and the boundary layer region. In regions 1 and 2 all the zero-order parameters are independent of x , and thus, x dependence of the perturbations can be assumed to be of the form

$$\delta x_1 = e^{ik_{x1}x}, \quad x \leq -h, \quad (4)$$

$$\delta x_2 = e^{ik_{x2}x}, \quad x \geq h. \quad (5)$$

The solutions in regions 1 and 2 have been so chosen that perturbations vanish at $+\infty$ and $-\infty$. The analysis is restricted to unstable perturbations, where $\omega_i > 0$. Boundary conditions corresponding to a tangential discontinuity, namely, continuity of the displacement and total pressure are applied to the boundaries at $x = \pm h$, result in the following matching conditions:

$$\chi_1 \frac{d\delta x_1}{dx} = \chi_{bl} \frac{d\delta x_{bl}}{dx}, \quad \delta x_1 = \delta x_{bl}, \quad x = -h \quad (6)$$

$$\chi_{bl} \frac{d\delta x_{bl}}{dx} = \chi_2 \frac{d\delta x_2}{dx}, \quad \delta x_{bl} = \delta x_2, \quad x = h. \quad (7)$$

The subscripts 1 and 2 correspond to regions 1 and 2, respectively. The boundary layer values are symbolized as δx_{bl} and k_{xbl} .

The eigenvalues of equation (3) are computed numerically using a standard shooting method adapted to our problem from Numerical Recipes [Press et al., 2002]. In this method, initial guess of an eigenvalue ω is chosen. The values of δx_1 and δx_2 are calculated using equations (4) and (5) and provided at two boundaries $\pm h$ as initial values of δx in equation (1). Then, δx_{bl} is calculated by integration with fifth-order Cash-Karp Runge-Kutta method, to the center of the boundary layer, from both sides of the boundary. In Fifth-order

Perturbations are assumed to be of the form $\delta g(\mathbf{r}, t) = g(x)e^{i(\mathbf{k}_t \cdot \mathbf{r} - \omega t)}$, where g is any perturbed quantity, $g(x)$ is the corresponding amplitude, ω is the complex frequency, and $\mathbf{k}_t = (k_y, k_z)$ is the tangential wave number.

Linearization of the warm compressible ideal MHD equations results in the following equation for the amplitude of the plasma displacement, δx :

$$\frac{d}{dx} \left(\chi \frac{d\delta x}{dx} \right) - \Omega \delta x = 0. \quad (1)$$

The function Ω in equation (1) is defined as $\Omega = \rho_0 [\omega'^2 - (\mathbf{V}_A \cdot \mathbf{k}_t)^2]$, and $\chi = -\Omega / k_x^2$. k_x is the complex wave number normal to the boundary, defined by

$$k_x = \left(\omega'^4 / \left[\omega'^2 (V_A^2 + C_S^2) - (\mathbf{V}_A \cdot \mathbf{k}_t)^2 C_S^2 \right] - k_t^2 \right)^{1/2}. \quad (2)$$

Here $V_A = B_0 / \sqrt{\rho_0 \mu_0}$ is the Alfvén speed, $C_S = \sqrt{\gamma P_0 / \rho_0}$ is the sound speed, $\omega' = \omega - \mathbf{U}_0 \cdot \mathbf{k}$ is the Doppler-shifted frequency, μ_0 is the

Cash-Karp Runge-Kutta method the step size is adjusted by monitoring of local truncation error to ensure accuracy. The solutions are then matched at the center of the boundary layer, $x=0$. Only if the initial chosen value of ω is an eigenvalue will these two solutions be the same at $x=0$.

Normalized velocities $V_{01,02}$ are used such that $V_{01,02} = U_{01,02}/V_{A2}$, where the normalization is with respect to the Alfvén speed in region 2, V_{A2} . The value of V_{02} is set to zero, while the modes supported by several values of V_{01} are considered. Therefore, using the definition above, the flow speed value is equal to $V_{flow1} = V_{01}/2$ for region 1 and $V_{flow2} = -V_{01}/2$ for region 2. The transition layer thickness Δ_x is normalized by R_E , wave numbers by $1/\Delta_x$, and frequencies $\omega_{r,i}$ by V_{A2}/Δ_x . The background physical parameters are set such that $B_{01}/B_{02} = 1.25$, $\rho_{01}/\rho_{02} = 1$, $\beta_1 = 0.5$, and $\beta_2 = 1.4$. Here $\beta_{1,2} = (P_{01,02})/(B_{01,02}^2/2\mu_0)$ represent values of plasma beta on each side of the boundary. These chosen parameters may be applicable to the Earth's magnetopause [Hasegawa et al., 2006; Foullon et al., 2010; Hwang et al., 2011], BBF channel boundaries in the central plasma sheet [Angelopoulos et al., 1994; Grigorenko et al., 2012; Ma et al., 2012], and shear flow boundaries in the solar atmosphere [Andries and Goossens, 2001; Foullon et al., 2013; Ofman and Thompson, 2011; Nykyri and Foullon, 2013; Céccere et al., 2014]. The normalized tangential wave number is set along y —parallel to the background flow speed direction, $\mathbf{k}_t = (k_y, 0)$. The variation of KHI growth rates with $k_y\Delta_x$ is calculated for different values of V_{01} and background magnetic fields directions.

3. Results

In this section we present numerical results for cases with and without magnetic stress acting at the boundary where the KHI is initiated. The ambient parameters were defined in section 2, and only the direction of magnetic fields on either side of the flow boundary, θ_1 and θ_2 , and background flow velocities, V_{flow1} , V_{flow2} , are varied through the variation of V_{01} . Here θ_1 and θ_2 are the angles between the tangential wave number, k_y , and background magnetic fields, B_{01} and B_{02} , in region 1 and region 2, respectively. Since the tangential wave number is chosen along the direction of the background flow, θ_1/θ_2 also describes the angles between B_{01}/B_{02} and the background flow velocities, V_{flow1} , V_{flow2} .

Particular focus is placed on the effect of magnetic tension on the strength of KHI surface wave growth rates, and on the initiation of the emission of propagating magnetosonic waves after the KHI has developed on the boundary. For each configuration, the variation of KHI surface wave growth rates and the wave emission efficiency as a function of normalized tangential wave number, $k_y\Delta_x$, is investigated.

Since the focus of this paper is propagating MHD wave emission due to the KHI, we consider only cases for $M_{F2} > 1$, after which the wave emission may be possible. M_{F2} is the fast Mach number defined as $M_{F2} = V_{flow2}/V_{fast2}$ and

$$V_{fast2} = \left[\frac{1}{2} \left(V_{A2}^2 + C_{S2}^2 + \sqrt{(V_{A2}^2 + C_{S2}^2)^2 - 4V_{A2}^2 C_{S2}^2 \cos^2 \theta_2} \right) \right]^{1/2} \quad (8)$$

is the fast MHD wave phase speed in region 2. We restrict our analysis to perturbations propagating along the background flow velocity. Perturbations propagating in arbitrary directions have maximum growth rates that increase monotonically with the flow velocity [Baranov et al., 1992; Ruderman and Fahr, 1995]. This regime is left as a future study.

It is worth noting here that another type of instability known as the Resonant Flow Instability (RFI) is possible along a shear flow boundary in which the Alfvén speed varies continuously [Taroyan and Erdélyi, 2002, 2003; Taroyan and Ruderman, 2011]. The Alfvén speed is piecewise constant for the boundary layer chosen in this study, but the Doppler-shifted Alfvén frequency, $\omega'_{A1,A2} = \mathbf{V}_{A1,A2} \cdot \mathbf{k}_t - \mathbf{V}_{flow1,flow2} \cdot \mathbf{k}_t$, varies continuously due to the continuous variation of flow speed. Therefore, Alfvén resonance leading to RFI is possible depending on parameters of the boundary layer. A wave mode is subject to RFI if the Doppler-shifted frequency, $\omega'_{1,2} = \omega_r - \mathbf{V}_{flow1,flow2} \cdot \mathbf{k}_t$, matches one of the Alfvén frequencies, $\omega_{A1,A2} = \mathbf{V}_{A1,A2} \cdot \mathbf{k}_t$, in the respective region [Taroyan and Erdélyi, 2002; Taroyan and Ruderman, 2011]. For all the cases we considered, the matching condition required for the RFI to occur is not met, and so this instability is excluded from our analysis. To ensure that the KH threshold condition is always met, we have computed the lower critical speed under the long wavelength approximation. In this limit, the transition layer thickness is neglected and the flow speed in region 1 is taken everywhere constant. For all cases considered, the flow speed exceeds the long wavelength limit.

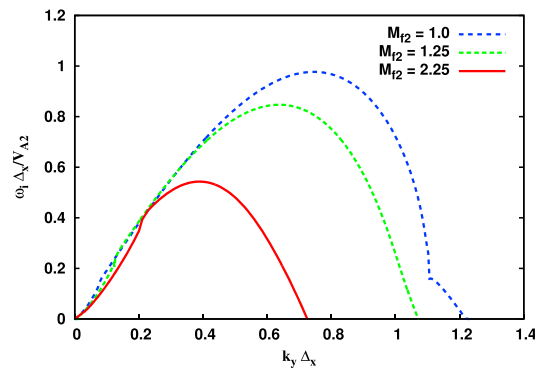


Figure 2. KHI waves growth rates dependence on the normalized tangential wave number, $k_y\Delta_x$, and fast Mach number, $M_{F2} = V_{01}/V_{fast2}$, $\theta_1 = \theta_2 = 90^\circ$. As M_{F2} increases, the growth rates decrease and $k_y\Delta_x$ values corresponding to the fastest growing modes are shifted to the left. The $k_y\Delta_x$ value beyond which all the modes are stable is also shifted to the left. Wave emission starts at $M_{F2} = 1.5$ for this configuration and is possible into both regions.

normalized growth rates first increase with $k_y\Delta_x$, reach a maximum and then decrease to zero. As M_{F2} increases, KHI surface wave growth rates and tangential wave numbers corresponding to maximum growth decrease—i.e., the wavelengths of the fastest growing modes increase. The value of the tangential wave number beyond which modes are stable also decreases with increasing M_{F2} . These results overall agree with previous studies [e.g., Walker, 1981; Miura and Pritchett, 1982; Gratton et al., 2004]. In these studies, however, flow speeds up to $M_{F2} = 2$ were considered with the argument that growth rates decrease considerably for values of $M_{F2} > 2$ [e.g., Miura and Pritchett, 1982].

We have investigated the possibility of magnetosonic wave emission by studying the properties of perturbed density eigenmodes. In the analysis the wave frequencies and hence the wave numbers are complex such that in general the eigenmodes contain both real and imaginary parts. We confine ourselves to considering eigenmode with envelopes which decay away from the boundary, but depending on the ratio of the real and imaginary wave numbers can propagate away from the shear flow generation region. There are limiting cases where the density eigenmodes fall into two categories: vortex-type structures confined to the transition layer and plane waves that carry energy available in the shear flow to large distances, $\gtrsim 10 R_E$, from the boundary. The latter corresponds to wave emission with the wave amplitude decreasing with distance from the generation region. We restrict our investigation to the KHI waves with normalized growth rates $\omega_i\Delta_x/V_{A2} \geq 0.02$ for the wave emission to be physically important.

Using above criteria, we find that in the absence of magnetic tension, propagating MHD wave emission due to the action of the KHI at the shear flow boundary is present at flow speed values of $M_{F2} = 2.25$. Figure 3 displays this fact showing density profiles for (a) $V_{01} = 1.25$ and (b) $V_{01} = 2.25$; the normalized tangential wave number $k_y\Delta_x = 0.9$ for Figure 3a and $k_y\Delta_x = 0.8$ for Figure 3b. MHD wave emission is not seen in Figure 3a, while it is clearly present propagating into both regions in Figure 3b. For this configuration, MHD wave emission starts at flow speed value of $M_{F2} = 1.5$ (see supporting information). For flow speed values corresponding to $M_{F2} < 1.5$, MHD wave emission is found not to be possible although growth rates are larger. These results suggest that not necessarily the largest growing KHI surface modes are the most significant modes on a KH unstable boundary. In contrast, growing modes of the KHI characterized by the emission of magnetosound can be more important. These magnetosonic waves will propagate into both regions and provide a significant source of energy transport.

As an aid to understanding the physical reason behind MHD wave emission on a KH unstable MHD shear flow boundary, the real and the imaginary wave numbers perpendicular to the boundary are calculated using equation (2). Figure 4 shows normalized values of perpendicular wave numbers, $k_{x,r,i}\Delta_x$, as a function of $k_y\Delta_x$ for flow speed values corresponding to the M_{F2} values in Figure 2. Figures 4a and 4b display the real and the imaginary wave numbers normal to the boundary in region 1, and Figures 4c and 4d show the real and the

3.1. KHI Surface Waves Growth Rates and MHD Wave Emission in the Absence of Magnetic Tension

The calculations presented in this section show the KHI surface wave growth rates and magnetosonic wave emission process for the case in which B_{01} and B_{02} are perpendicular to the shear flow boundary and tangential wave number, i.e., $\theta_1 = \theta_2 = 90^\circ$. This removes the effect of magnetic tension on the shear flow boundary, since the tangential components of the magnetic field are zero on either side. RFI is found not to be possible in this configuration Taroyan and Erdelyi, [2002, 2003]; therefore, KHI is the only possible instability.

Figure 2 shows the growth rates of KHI surface waves as a function of normalized tangential wave number, $k_y\Delta_x$. Three different values of the flow speed, V_{flow1} , are chosen corresponding to $M_{F2} = 1, 1.25, \text{ and } 2.25$. As displayed in Figure 2,

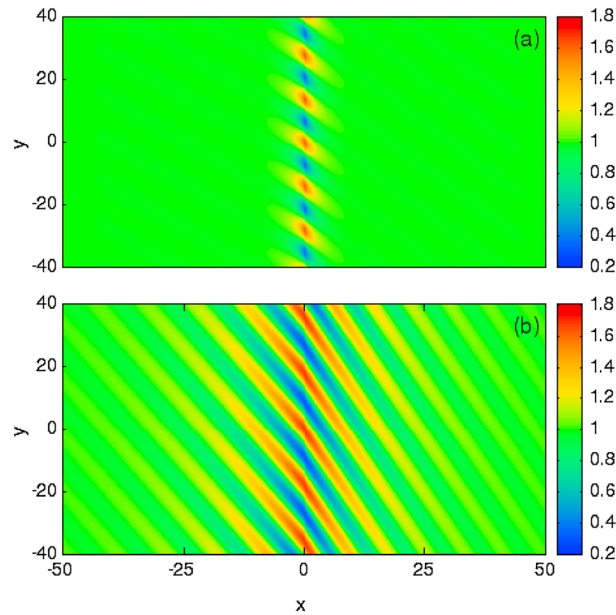


Figure 3. Density profiles corresponding to Figure 2; (a) $M_{F2}=1.25$ and (b) $M_{F2}=2.25$. The normalized tangential wave number $k_y \Delta_x = 0.9$ for Figure 3a and $k_y \Delta_x = 0.8$ for Figure 3b. It is visible that waves propagate into region 1 and region 2 in Figure 3b, while no propagation is observed in Figure 3a. The flow speed values corresponding to $M_{F2} < 1.5$ did not result wave propagation into either region.

imaginary wave numbers normal to the boundary in region 2. The real part of the perpendicular wave numbers represents the physical wavelength and the imaginary part represents the rate of the spatial decay away from the boundary. As seen in Figures 4a and 4b, for flow velocity values corresponding to $M_{F2} < 2.25$ the real parts of the perpendicular wave numbers, k_{x1r} , are small while the imaginary parts, k_{x1i} , are large. This suggests that the waves are mainly surface type, i.e., have strong spatial decay and confined to the boundary for $M_{F2} < 2.25$. For flow speed value where $M_{F2} = 2.25$, however, k_{x1r} picks up larger values while k_{x1i} becomes smaller, which suggests that waves change their dominant character into propagating modes and carry energy away from the boundary into region 1. Figures 4c and 4d show that in region 2 the real/imaginary parts of the perpendicular wave numbers show similar characteristics to those of region 1. We have calculated the absolute values of the ratio of the real part to the imaginary part of the perpendicular wave numbers and can hence define the characteristics of wave emission in terms of this ratio. For example, in cases where $k_{xi}/k_{xr} = 0.1$ then the eigenmode experiences one spatial e -fold amplitude decay in 10 wavelengths. To make comparisons in physical units, we can also calculate the magnitude of this ratio which leads to a decay length of based on decay length

characteristics of wave emission in terms of this ratio. For example, in cases where $k_{xi}/k_{xr} = 0.1$ then the eigenmode experiences one spatial e -fold amplitude decay in 10 wavelengths. To make comparisons in physical units, we can also calculate the magnitude of this ratio which leads to a decay length of based on decay length

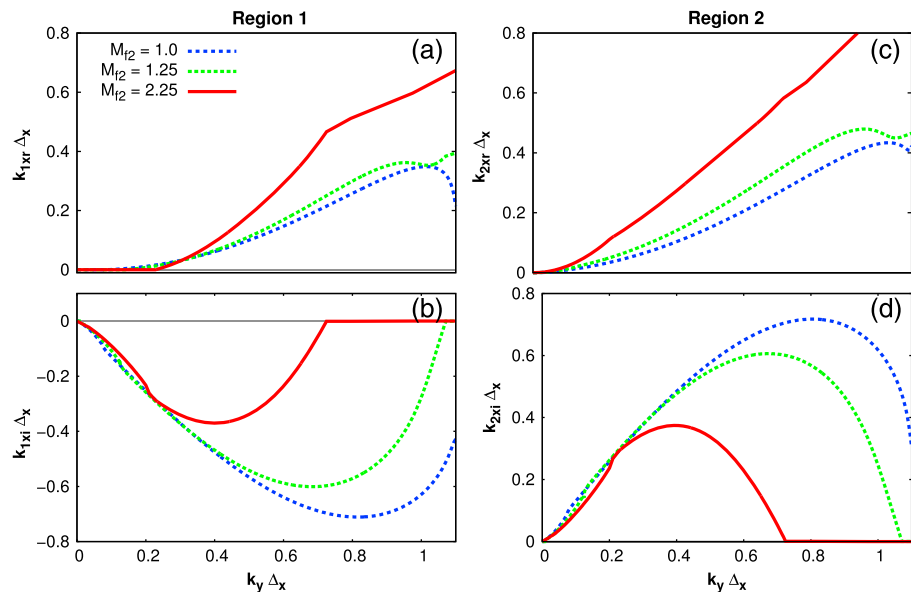


Figure 4. Dependence of normalized perpendicular wave numbers on M_{F2} and $k_y \Delta_x$ —the background parameters are the same as in Figure 2. The (a) real/(b) imaginary parts of perpendicular wave numbers in region 1; (c) real/(d) imaginary parts of perpendicular wave numbers in region 2. For $M_{F2} < 2.25$ both regions have large imaginary wave numbers, Figures 4b and 4d, showing a strong decay and no propagation into either region. The real parts of the wave numbers become larger, while the imaginary parts become smaller for $M_{F2} = 2.25$, showing the possibility of wave propagation.

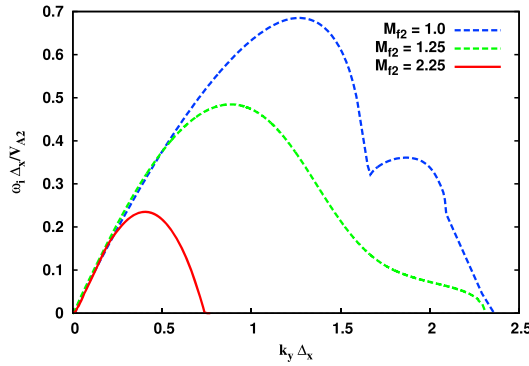


Figure 5. Growth rate versus $k_y \Delta_x$ for $\theta_1 = 60^\circ, \theta_2 = 30^\circ$. KHI growth rates are smaller than the $\theta_1 = \theta_2 = 90^\circ$ case due to the effect of the magnetic tension on the boundary. Emission of MHD waves, however, starts at smaller flow speed values—for $M_{F2} \geq 1.25$.

and 30° , respectively. This will result in stronger magnetic tension in region 2 due to a larger parallel magnetic field component. We have first calculated the lower cutoff speed for this configuration under the assumption of large wavelength and zero transition thickness and found it to be $M_{F2} \geq 1.0$. Then we have excluded possible RFI waves by only considering flow speeds larger than 1.0. Figure 5 shows the variation of KHI surface wave growth rates as a function of $k_y \Delta_x$ for this configuration, and for same values of M_{F2} that were used to obtain Figure 2. The variation of the growth rates with $k_y \Delta_x$ is the same as $\theta_1 = \theta_2 = 90^\circ$ case. However, as a result of increased magnetic tension, KHI growth rates decrease, which agrees with previous results [Miura and Pritchett, 1982].

Density profiles, for $\theta_1 = 60^\circ$ and $\theta_2 = 30^\circ$, are shown in Figures 6a and 6b. Figure 6a is for $k_y \Delta_x = 1.8$ and $M_{F2} = 1.0$, and 6b is for $k_y \Delta_x = 1.8$ and $M_{F2} = 1.25$. As displayed in Figure 6a the KHI waves are mainly confined along shear flow boundary, while they can propagate to distances $\geq 25R_E$ into region 2 in Figure 6b.

Figure 7 shows the real and the imaginary parts of perpendicular wave numbers in (a and b) region 1 and (c and d) region 2, for the same M_{F2} values used to obtain Figure 5. Similar to $\theta_1 = \theta_2 = 90^\circ$ configuration,

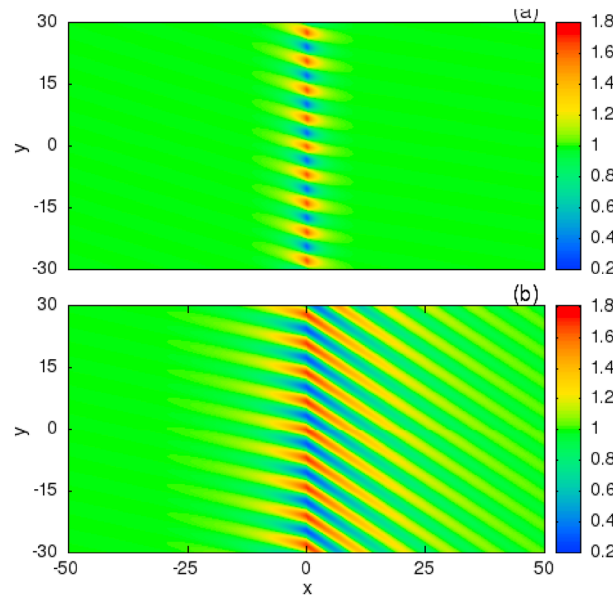


Figure 6. Density profiles for $\theta_1 = 60^\circ, \theta_2 = 30^\circ$. (a) $M_{F2} = 1.0$ and $k_y \Delta_x = 1.8$; (b) $M_{F2} = 1.25$ and $k_y \Delta_x = 1.8$. While wave emission is not visible in Figure 6a, Figure 6b shows emission of MHD waves mainly into region 2.

of $\geq 10R_E$, in order to investigate wave emission criteria for each region. The real part of the perpendicular wave numbers must be sufficiently large for KHI waves to be able to propagate into either region. We find that waves are emitted into region 1 and reach distances $\geq 10R_E$ away from the boundary if $k_{x1r}/k_{x1i} \geq 0.3$ and into region 2 if $k_{x2r}/k_{x2i} \geq 0.75$. For stronger wave emission, however, where the magnetosonic waves can propagate into distances $\geq 25R_E$, the values of k_{xr}/k_{xi} must be ≥ 1 .

3.2. KHI Surface Waves Growth Rates and MHD Wave Emission Under the Effects of Magnetic Tension

Magnetic tension effects are now included by changing the values of θ_1 and θ_2 to 60°

and 30° , respectively. This will result in stronger magnetic tension in region 2 due to a larger parallel magnetic field component. We have first calculated the lower cutoff speed for this configuration under the assumption of large wavelength and zero transition thickness and found it to be $M_{F2} \geq 1.0$. Then we have excluded possible RFI waves by only considering flow speeds larger than 1.0. Figure 5 shows the variation of KHI surface wave growth rates as a function of $k_y \Delta_x$ for this configuration, and for same values of M_{F2} that were used to obtain Figure 2. The variation of the growth rates with $k_y \Delta_x$ is the same as $\theta_1 = \theta_2 = 90^\circ$ case. However, as a result of increased magnetic tension, KHI growth rates decrease, which agrees with previous results [Miura and Pritchett, 1982].

Density profiles, for $\theta_1 = 60^\circ$ and $\theta_2 = 30^\circ$, are shown in Figures 6a and 6b. Figure 6a is for $k_y \Delta_x = 1.8$ and $M_{F2} = 1.0$, and 6b is for $k_y \Delta_x = 1.8$ and $M_{F2} = 1.25$. As displayed in Figure 6a the KHI waves are mainly confined along shear flow boundary, while they can propagate to distances $\geq 25R_E$ into region 2 in Figure 6b.

Figure 7 shows the real and the imaginary parts of perpendicular wave numbers in (a and b) region 1 and (c and d) region 2, for the same M_{F2} values used to obtain Figure 5. Similar to $\theta_1 = \theta_2 = 90^\circ$ configuration, wave propagation into regions 1 and 2 at distances $\geq 10R_E$ is possible for $k_{x2r}/k_{x2i} \geq 0.75$ and $k_{x1r}/k_{x1i} \geq 0.3$. More significant KHI magnetosonic wave emission at distances $\geq 25R_E$ is possible only if $k_{x1r,x2r}/k_{x1i,x2i} \geq 1$. However, these conditions are met at low velocity $M_{F2} = 1.25$, which is lower than $\theta_1 = \theta_2 = 90^\circ$ case. Therefore, as magnetic tension increases, flow velocity, at which MHD wave emission starts, decreases. The results displayed in Figures 5–7 suggest that increased magnetic tension is favorable for MHD wave emission due to KHI. Likely the inhibition of KHI surface wave growth rates by magnetic tension may contribute to the increasing dominance of the emitted wave.

3.3. MHD Wave Emission Thresholds: Relation to Wave Numbers and Phase Velocities

In this section, the phase speed values of the KHI unstable waves are calculated using

$$\mathbf{U}_p = \frac{\omega_r}{(k_t^2 + k_x^2)} \mathbf{k}_r. \quad (9)$$

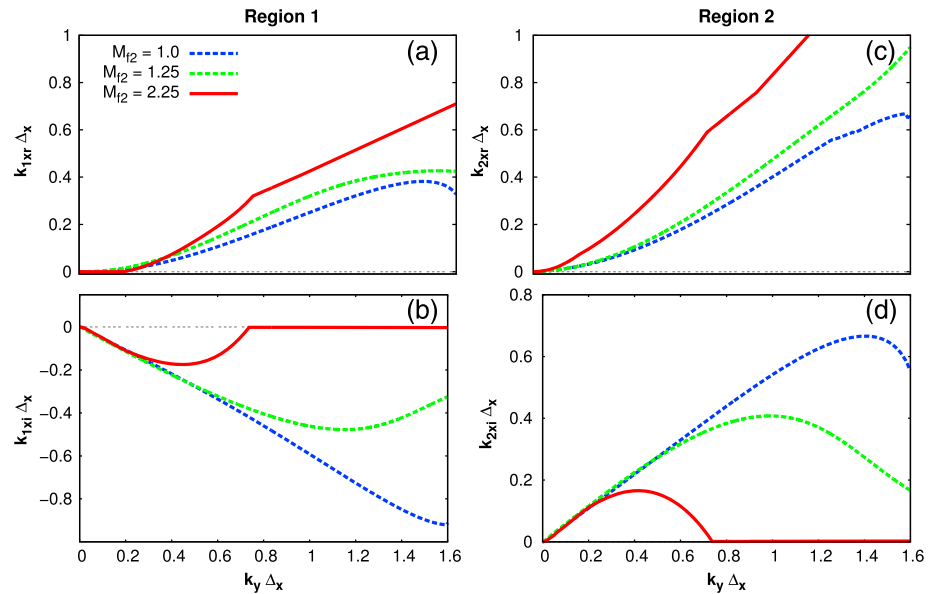


Figure 7. Perpendicular wave numbers versus $k_y \Delta_x$ for $\theta_1 = 60^\circ, \theta_2 = 30^\circ$. (a and b) The perpendicular wave numbers for region 1, k_{x1r}, k_{x1i} ; (c and d) the wave numbers for region 2, k_{x2r}, k_{x2i} . Smaller/larger values of the real/imaginary wave numbers in Figure 7a/7b reveal the fact that wave propagation into region 1 is weaker than into region 2.

Comparison of normalized phase speeds, $V_p = U_p/V_{A2}$, is shown in Figures 8a and 8b for $\theta_1 = \theta_2 = 90^\circ$ and Figures 8c and 8d for $\theta_1 = 60^\circ, \theta_2 = 30^\circ$. Flow speed values are the same as in Figures 2 and 5. The normalized phase speed of fast MHD waves, $V_{fast1,2}$, in the absence of flow are also shown for comparison (grey and brown lines).

Figure 8 shows that the phase speed values of the KHI waves are in the expected range of fast MHD waves. This is consistent with the results of *Turkakin et al.* [2013], where it is shown that the fastest growing KHI modes, i.e., primary KHI modes, are fast MHD waves.

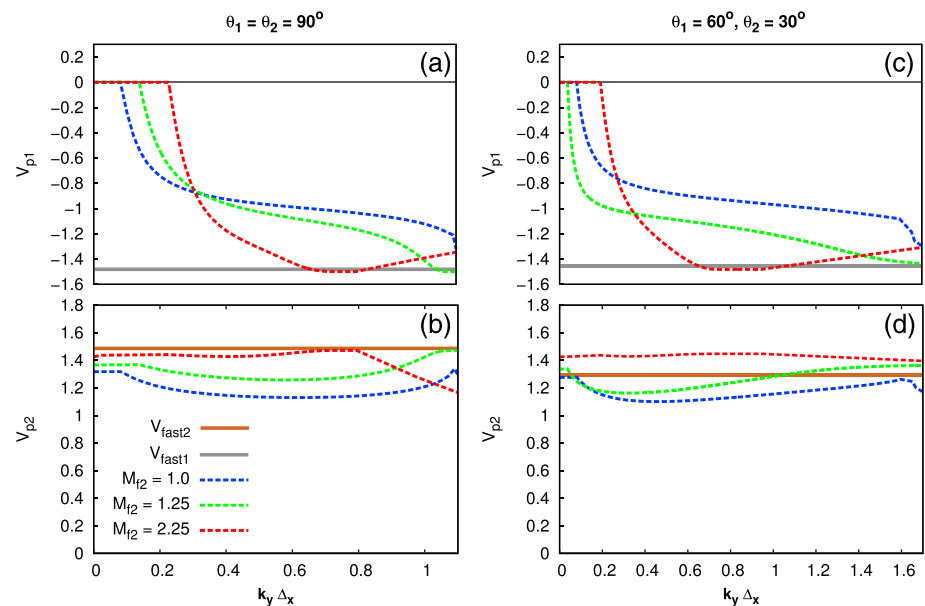


Figure 8. Phase velocities versus $k_y \Delta_x$ for (a and b) $\theta_1 = \theta_2 = 90^\circ$ and (c and d) $\theta_1 = 60^\circ, \theta_2 = 30^\circ$. Flow speed values are the same as in Figures 2 and 5. Phase speed values of fast MHD waves in the absence of flow, V_{fast1}, V_{fast2} , are shown for comparison (grey and brown lines). At flow speed values $M_{F2} = 2.25$, wave propagation is possible into both regions for $\theta_1 = \theta_2 = 90^\circ$ and $\theta_1 = 60^\circ, \theta_2 = 30^\circ$. Phase velocity of KHI waves reach or exceed the fast MHD wave phase speeds when wave propagation is obtained into either region.

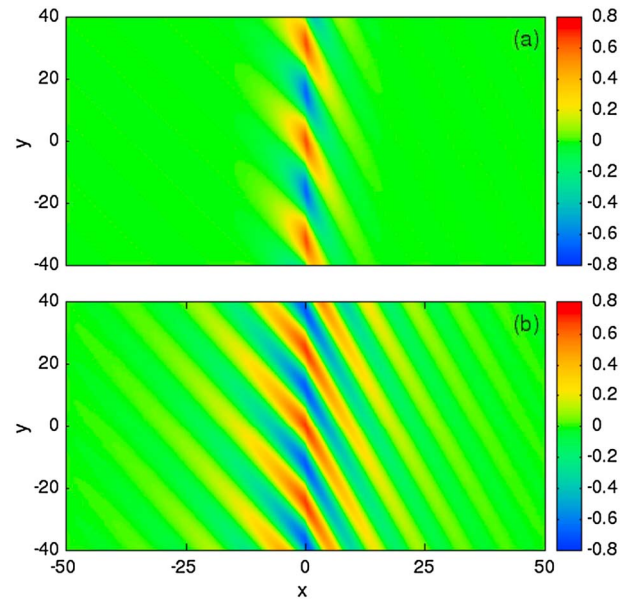


Figure 9. Density profiles for magnetic field configuration $\theta_1 = \theta_2 = 60^\circ$. While wave emission is not seen in Figure 9a, waves visibly propagate into region 1 and region 2 in Figure 9b: $M_{F2} = 2.5$; (a) $k_y \Delta_x = 0.4$ and (b) $k_y \Delta_x = 0.5$. While there is no wave emission at wavelengths corresponding to $k_y \Delta_x = 0.4$ into either region, at wavelengths corresponding to $k_y \Delta_x = 0.5$ waves are emitted into both region 1 and region 2, at distances $\lesssim 25R_E$. Above Figure display the fact that for a specific configuration, not all the wavelengths can be emitted from a KH unstable boundary.

Figures 8a and 8b shows that for the $\theta_1 = \theta_2 = 90^\circ$ case, the phase speeds of KHI surface waves reach and exceed the values of fast wave phase speeds in region 1 and region 2 only for $M_{F2} = 2.25$. The phase speeds reach the fast MHD wave phase speeds at normalized wave number values, $k_y \Delta_x$, corresponding to the start of wave emission into each region.

Figures 8c and 8d in show that the phase speeds of KHI surface waves do not reach or exceed the fast MHD wave phase speeds in both regions at flow speed values, $M_{F2} \lesssim 1.25$ for $\theta_1 = 60^\circ$, $\theta_2 = 30^\circ$ configuration.

The results shown in Figures 8a–8d suggest that MHD wave emission starts at $k_y \Delta_x$ values where the KHI wave phase speeds reach or exceed the fast MHD wave phase speeds in either media. In the presence of a strong magnetic tension, however, for sufficiently high flow speeds, the KHI waves phase speeds may greatly exceed the fast wave phase speeds at all values of $k_y \Delta_x$, which shows that waves have large phase speeds even when they are purely surface waves. Therefore, reaching or exceeding the fast MHD wave phase speeds is a necessary, but not sufficient, condition for wave emission from a KH unstable MHD shear flow boundary.

Another important fact about wave emission driven by KHI at a shear flow boundary is illustrated in Figures 9 and 10 for $\theta_1 = \theta_2 = 60^\circ$ and $M_{F2} = 2.5$. The lower cutoff speed for this configuration under large wavelength and zero transition thickness assumption is calculated as $M_{F2} \geq 0.8$. Therefore, $M_{F2} = 2.5$ value is well above the KHI lower cutoff speed and possibility of RFI waves are excluded for this magnetic field configuration as well. Figure 9 shows the density perturbation profile for this configuration for (a) $k_y \Delta_x = 0.4$ and (b) $k_y \Delta_x = 0.5$. Figure 9a displays the fact that at $k_y \Delta_x = 0.4$, the wave emission is not present. When the value of $k_y \Delta_x$ increases to 0.5, however, MHD waves can propagate into both region 1 and region 2, as far as $\lesssim 25R_E$ (see Figure 9b). The results shown in this Figure 9 suggest that a certain wavelength regime exists for each region, where KHI waves are emitted.

KHI wave growth rates, phase velocities, and perpendicular wave numbers corresponding to values used in Figures 9a and 9b are shown in Figures 10a–10c. Figure 10a shows growth rates (red solid line) and phase velocities of waves in regions 1 and 2 (green and blue dashed lines) with the left vertical axis corresponding to phase speed values and the right vertical axis corresponding to growth rates. Background values of the fast MHD wave phase speeds in region 1 and region 2 are also shown for comparison (grey and brown solid lines). Figures 10b and 10c show the real and the imaginary perpendicular wave numbers (blue and green dashed lines) for region 1 and region 2, respectively. In Figures 10b and 10c the left vertical axes show the imaginary

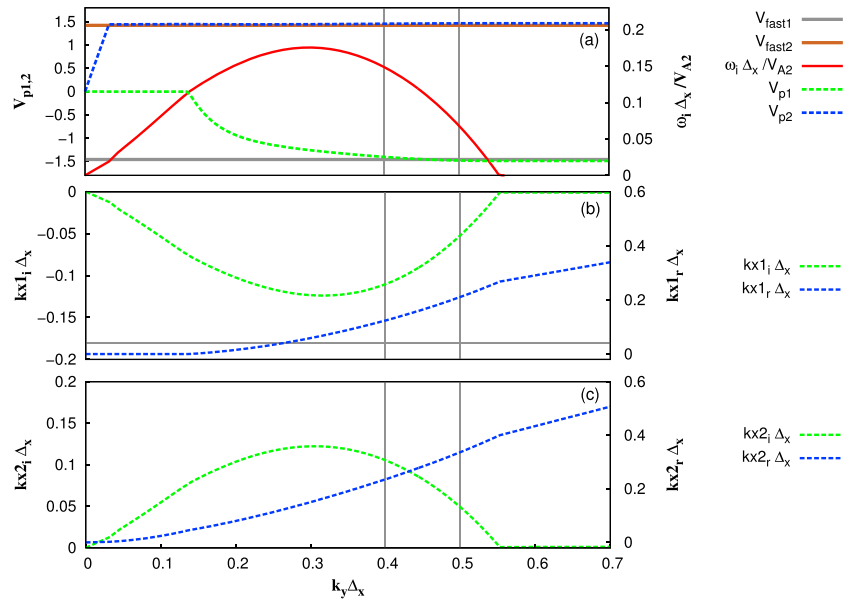


Figure 10. Comparison of KHI waves phase velocities, growth rates, and the real and the imaginary perpendicular wave numbers corresponding to Figure 9. Vertical grey lines mark the position of $k_y \Delta_x = 0.4$ and $k_y \Delta_x = 0.5$ corresponding to Figures 9a and 9b. (a) The growth rates with phase speed values of KHI waves; (b and c) the real and the imaginary wave numbers for region 1 and region 2. In Figure 10a the values of fast MHD wave phase speeds in the absence of flow are also shown for region 1 and region 2 (grey and brown lines). The absolute values of $k_{x1r}/k_{x1i} < 0.3$ and $k_{x2r}/k_{x2i} < 0.75$ at wavelengths corresponding to $k_y \Delta_x = 0.4$, where wave emission into either region is not found (see Figure 9a). At wavelengths corresponding to $k_y \Delta_x = 0.5$, where wave emission is seen in Figure 9b, the absolute value of $k_{x1r}/k_{x1i} > 0.3$ and $k_{x2r}/k_{x2i} > 0.75$, which agrees with the results found for $\theta_1 = \theta_2 = 90^\circ$ and $\theta_1 = 60^\circ, \theta_2 = 30^\circ$ configurations.

and right vertical axes show the real parts of the perpendicular wave numbers. Vertical grey lines mark the values of $k_y \Delta_x = 0.4$ and 0.5 corresponding to Figures 9a and 9b, respectively.

Comparing Figure 10a to Figure 9a, it can be seen that at the start of the region characterized by the emission of propagating magnetosound, the growth rates decrease with increasing $k_y \Delta_x$. The fact that wave emission starts at normalized tangential wave number or wavelength values, where growth rates are decreasing, is also obtained for the magnetic field configurations $\theta_1 = \theta_2 = 90^\circ, \theta_1 = 60^\circ, \theta_2 = 30^\circ$.

Similar to the previous cases considered, the values of KHI wave phase velocities in Figure 10a show that at the points of MHD wave emission (vertical grey lines) the phase speeds of the waves reach or exceed the background fast MHD wave phase speeds. Figures 10b and Figures 10c show that at wavelengths corresponding to $k_y \Delta_x = 0.5$, where wave emission starts, the real parts of perpendicular wave numbers, k_{x1r}, k_{x2r} , become large and the imaginary parts, k_{x1i}, k_{x2i} , become small. The absolute values of $k_{x1r}/k_{x1i} > 0.3$ and $k_{x2r}/k_{x2i} > 0.75$ for this value of wave number, which agrees with the condition for wave emission discussed in sections 3.1 and 3.2.

3.4. The Effects of Magnetic Field Rotation in the Flowing Region

In this section we investigate the variation of KHI wave growth rates and the absolute values of k_{x1r}/k_{x1i} and k_{x2r}/k_{x2i} , as the direction of the magnetic field in region 1 is changed. The direction of the magnetic field in region 1, θ_1 , varies from $0 - \pi$, while the direction of the magnetic field in region 2, θ_2 , is set to a constant value. Resulting values of growth rates, k_{x1r}/k_{x1i} and k_{x2r}/k_{x2i} are shown in Figures 11a–11c for four chosen values of $\theta_2 = 0^\circ, 30^\circ, 60^\circ$, and 90° . The flow velocity is chosen such that $M_{F2} = 2.25$ and $k_y \Delta_x = 0.5$, where, as suggested by the results in previous sections, the KHI wave emission into either region is expected to be possible, at least for some of the magnetic field configurations.

Figure 11a shows that as θ_1 varies from $0 - \pi$ the growth of KHI surface waves increases to reach a maximum at $\theta_1 = 90^\circ$ and decrease thereafter. The growth rate profiles are similar for all θ_2 values considered, while the magnitudes of growth rates become larger as θ_2 increases; i.e., magnetic tension along the shear flow boundary decreases. This supports the conclusion that strong magnetic tension works against the growth of the KHI. Figures 11b and 11c show the absolute values of k_{x1r}/k_{x1i} and k_{x2r}/k_{x2i} , respectively. The ratio of k_{x1r}/k_{x1i}

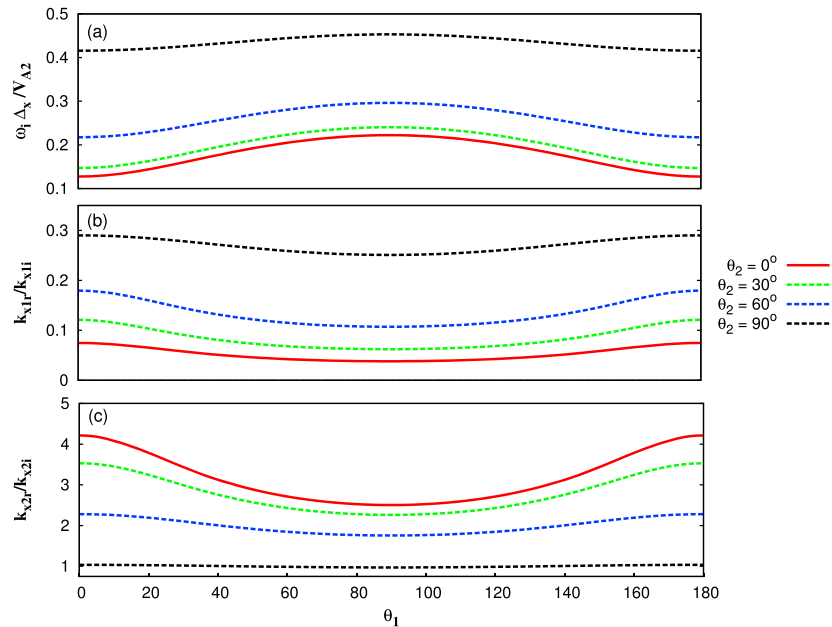


Figure 11. Comparison of KHI waves growth rates, and the ratio of the real (k_{x1r}, k_{x2r}) to the imaginary (k_{x1i}, k_{x2i}) perpendicular wave numbers in region 1 and region 2 as θ_1 varies from $0 - \pi$. $M_{F2} = 2.25$, $k_y \Delta_x = 0.5$, and θ_2 is chosen as $0^\circ, 30^\circ, 60^\circ$, and 90° . (a) Growth rates reach the maximum at $\theta_1 = 90^\circ$ and decreases to their initial values at $\theta_1 = 180^\circ$. (b and c) As θ_1 approaches to 90° , k_{x1r}/k_{x1i} and k_{x2r}/k_{x2i} decrease, showing that KHI waves are more evanescent. Therefore, MHD wave emission is less efficient, while KHI growth is the largest at values $\theta_1 \sim 90^\circ$. If present, KHI wave emission would be most efficient for $\theta_1 \simeq 0^\circ - 30^\circ$ and $\theta_1 \simeq 150^\circ - 180^\circ$, where k_{x1r}/k_{x1i} and k_{x2r}/k_{x2i} values increase with propagation into region 2 being much stronger than into region 1.

decreases as θ_1 increases from 0° to 90° , reaches a minimum at $\theta_1 = 90^\circ$, and then increases to their initial value at $\theta_1 = 180^\circ$. The ratio of k_{x1r}/k_{x1i} does not exceed the value 0.3 that resulted in wave emission into region 1 to distances $\gtrsim 10R_E$ in cases discussed above. Therefore, for all θ_1 and θ_2 values considered here, with the flow velocity $M_{F2} = 2.25$ and $k_y \Delta_x = 0.4$, KHI wave emission into region 1 is found not to be possible. The increase in the absolute values of k_{x1r}/k_{x1i} , where $\theta_1 \lesssim 30^\circ$ and $\theta_1 \gtrsim 150^\circ$, suggests that for bigger flow speed and $k_y \Delta_x$ values, KHI wave emission into region 1 may be possible at these values of θ_1 . For θ_1 values that are close to $\simeq 90^\circ$, k_{x1r}/k_{x1i} values are very small for all chosen values of θ_2 , suggesting that KHI wave emission into region 1 will always be either very weak or not possible. k_{x2r}/k_{x2i} values show the same characteristics as k_{x1r}/k_{x1i} in terms of variations with θ_1 . The absolute values of $k_{x2r}/k_{x2i} > 1.0$ for all values of θ_1 and θ_2 , which shows that KHI wave emission into region 2 is possible for all the magnetic field configurations and parameters considered here the waves can reach distances $\simeq 25R_E$.

The results presented in Figure 11 overall suggest that while the growth rates of the KHI waves increase to a maximum at $\theta_1 = 90^\circ$, modes that support propagating wave emission are not favorable since they have strong spatial decay, i.e., large imaginary parts of perpendicular wave numbers, k_{x1i}, k_{x2i} . Larger values of $k_{x1r}/k_{x1i}, k_{x2r}/k_{x2i}$ for $\theta_1 \simeq 0^\circ - 30^\circ$ and $\theta_1 \simeq 150^\circ - 180^\circ$ suggest that these configurations are more favorable for emission of propagating MHD waves from KH unstable boundary. This is due to the effect of magnetic tension on the boundary provided by the components of the magnetic fields parallel or antiparallel to the flow and the boundary. As the value of θ_2 increases, the KHI wave growth rates also increase, while overall variations with θ_1 stay the same.

3.5. Applications to Shear Flow Boundaries in the Earth's Magnetosphere and the Solar Corona

We will now discuss our results in connection with the context of shear flow regions in Earth's magnetosphere and in the solar corona. Although magnetic fields, densities, and flow velocities are various in these regions, certain common characteristics hold.

If we consider Earth's magnetopause boundary, flow is large in the magnetosheath region, while the strengths and directions of the magnetic fields vary depending on the point of observation [Nakai and Ueno, 2011;

Hwang et al., 2011; Foullon et al., 2008; Hasegawa et al., 2006]. In Figure 1, region 1 approximates the magnetosheath, and region 2 the magnetosphere. Using observational values in [Nakai and Ueno, 2011; Hwang et al., 2011; Fairfield et al., 2000; Hasegawa et al., 2006], we have calculated M_{F_2} to vary between ≈ 0.5 and 1.2 in the dayside region and ≈ 0.5 and 3.5 in the nightside and magnetotail regions. Therefore, flow speeds corresponding to $M_{F_2} > 1$ are physically possible along the magnetopause boundary, which means emission of magnetosonic waves is feasible. Ambient magnetic fields configuration corresponding to $\theta_1 = \theta_2 = 90^\circ$ is applicable to the dayside magnetopause when the IMF is purely northward or southward. Under these conditions our results suggest that on the dayside magnetopause, the KH surface wave growth is possible with large growth rates. Energy propagation into the magnetosphere would not be very efficient due to the lack of modes supporting the emission of MHD waves in this configuration. A configuration with $\theta_1 = 60^\circ$ and $\theta_2 = 30^\circ$, however, is also possible on the dayside magnetopause, in which case very efficient wave emission into the magnetosphere may occur (see Figure 6). Along the dawn and dusk flanks and into the nightside magnetopause, the magnetic fields on either side of the boundary usually become increasingly parallel or antiparallel to each other [e.g., Hasegawa et al., 2006; Nakai and Ueno, 2011]. The nightside magnetopause and dawn and dusk flanks are therefore favorable for emission of MHD waves since a strong magnetic tension will generally be present, which enhances wave emission from a KH unstable flow boundary.

In the central plasma sheet of Earth's magnetotail, Bursty Bulk Flow (BBF) channel boundaries may also be subject to the KHI and MHD wave emission [Turkakin et al., 2014]. At the edges of BBF flow channels, region 1 would correspond to inside and region 2 would correspond to outside of the channel. Bursty Bulk Flows (BBFs) usually form at $\approx 19R_E$ in the magnetotail and move toward the Earth decelerating and stopping at $\approx 6R_E$ [e.g., McPherron et al., 2011]. The flow speed in BBFs varies between 200 and 1500 km/s [e.g., Angelopoulos et al., 1997; Shiokawa et al., 1997]. Using observations [Angelopoulos et al., 1992; Volwerk et al., 2007; Ma et al., 2012], BBF speeds normalized by the phase speed of the fast MHD wave in the region outside of the channel are calculated to vary between 0.2 and 2.5, implying that the KHI and modes supporting MHD wave emission can be excited along these shear flow boundaries. Magnetic fields are parallel to the BBF channel boundary in the far magnetotail and change direction due to geomagnetic field dipolarization as BBFs move closer to Earth. In other words θ_1 and θ_2 increase as BBFs move closer to Earth. Results presented in Figure 11 then suggest that on BBF channel boundaries, the KHI growth is more efficient at positions closer to Earth and wave emission is more efficient farther from Earth. Strong emission of MHD waves due to the KHI at positions farther away from Earth may be able to transfer available energy out of BBF channels, resulting in deceleration and stopping of BBFs in near-Earth regions [Turkakin et al., 2014]. Due to larger values of magnetic fields and thus magnetic tension, propagating MHD wave emission due to the KHI would be more observable along BBF channel boundaries than along the magnetosphere boundary. This can explain often observed kink and sausage wave oscillations emitted from BBF channel boundaries that propagate toward the magnetotail flanks [Sergeev et al., 2004; Volwerk et al., 2005; Zhang et al., 2005].

KHI-driven propagating MHD wave emission may also be possible on the shear flow boundaries of coronal plumes, Supra-Arcade Downflows (SADs), coronal mass ejections (CMEs), and coronal streamers. Although magnetic field strengths and plasma densities are considerably larger in the solar corona, plasma beta values are of order 1 [Foullon et al., 2013; Feng et al., 2013; Nykyri and Foullon, 2013] and normalized values used in this paper are still applicable. Numerical studies of the KHI on the boundaries of CMEs [Foullon et al., 2011; Ofman and Thompson, 2011; Nykyri and Foullon, 2013; Foullon et al., 2013; Mostl et al., 2013], SADs [Cecere et al., 2014], coronal plumes [Andries and Goossens, 2001], and coronal streamers [Feng et al., 2013] have used configurations similar to those used in the current study. Therefore, our results are applicable to analysis of these solar coronal regions.

SADs have strong similarities to BBF channels occurring in Earth's central plasma sheet [McKenzie and Savage, 2009; Cecere et al., 2014]. Cecere et al. [2014] investigated numerically the occurrence of the KHI on the boundaries of SADs but did not investigate the possibility of the KH-driven modes generating the emission of propagating fast magnetosonic modes. Similar to the breaking of BBFs suggested in Turkakin et al. [2014], propagating wave emission due to the KHI along SAD boundaries may be possible and can potentially explain observed deceleration of SADs. Coronal plumes and coronal streamer boundaries have similar characteristics to SADs [Andries and Goossens, 2001; Feng et al., 2013] and can thus support MHD wave emission as well. In fact, coronal streamer waves, which show very similar characteristics to the waves emitted from BBF channels, have been observed [Chen et al., 2010].

CME boundaries have similarities to the magnetopause boundary [Foullon *et al.*, 2011]. The magnetic field, however, has a helical configuration on one side and is smoothed out on the other side of a CME boundary. With high-resolution images provided by the Atmospheric Imaging Assembly (AIA) on board the Solar Dynamic Observatory (SDO), KHI waves along fast CME ejecta were detected [Foullon *et al.*, 2011; Ofman and Thompson, 2011; Foullon *et al.*, 2013] and numerically investigated [Ofman and Thompson, 2011; Nykyri and Foullon, 2013; Möstl *et al.*, 2013]. While Nykyri and Foullon [2013] and Ofman and Thompson [2011] studied the side of the CME boundary where magnetic fields are in a helical configuration, Möstl *et al.* [2013] considered the side where the helical configuration is smoothed. With the flow speed values chosen, they concluded that if there is a parallel component of the magnetic field of strength 20% of the background field, the KHI is stabilized.

Using observed values in Foullon *et al.*, 2011 [2011, 2013], Möstl *et al.* [2013], and Cécere *et al.* [2014], we have calculated the values of M_{F2} in solar coronal regions as varying between 0.5 and 2.0. The availability of sufficiently fast flow speeds $M_{F2} > 1$ implies that along shear flow boundaries in the solar corona the growth of KH modes supporting the emission of magnetosound may be possible. Since background magnetic fields tend to be parallel to the boundary of SADs [Cécere *et al.*, 2014], propagating wave emission due to the KHI will be more probable along these boundaries. In contrast, magnetic fields on CME boundaries usually have stronger perpendicular components [Ofman and Thompson, 2011; Foullon *et al.*, 2013; Nykyri and Foullon, 2013], and thus, KHI surface wave growth will be more favorable than KHI-driven propagating MHD wave emission. Nevertheless, on the side of the CME boundary where the magnetic field is smoothed, the available strong magnetic tension may support KH modes generating propagating wave emission if flow speeds corresponding to $M_{F2} > 1$ are reached. These emitted MHD waves on shear flow boundaries of the solar corona can play a significant role in energy transfer between different regions during solar eruptions.

4. Discussion and Conclusions

A theory has been developed to investigate the excitation of modes which cause the emission of magnetosonic waves due to the KHI on MHD shear flow boundaries. The parameters chosen are applicable to different shear flow boundaries in Earth's magnetosphere and the solar corona. We have determined threshold values of flow speed and tangential wave number for modes supporting MHD wave emission under different configurations of the background magnetic fields, $B_{01,02}$. Varying the background magnetic fields allowed us to investigate the effects of magnetic tension on wave emission due to the KHI. The dependence of the MHD wave emission on perpendicular wave numbers and phase velocity of the KHI waves has also been investigated.

It is found that the onset of the wave emission is usually at flow speed corresponding to $M_{F2} > 1$. As the component of the magnetic field parallel to the MHD shear flow boundary is increased on either side, the threshold values of the flow speed where the KHI can generate propagating MHD wave modes decreases. We have concluded that increasing magnetic tension leads to the generation of KHI modes which support propagating wave emission along the shear flow boundaries. While magnetic tension enhances the excitation of modes characterized by propagating wave emission, it hinders the growth of KH surface modes. Emission is more efficient into the region where there is a stronger magnetic field component parallel to the boundary, i.e., a stronger magnetic tension. Therefore, most of the energy available on the shear flow boundary will be carried into the region with stronger magnetic tension.

As described earlier, since the wave numbers are complex, the relative strength of the spatial decay in a number of wavelengths away from the boundary is defined by the ratio of the real and imaginary parts of the wave numbers in each region. We compute the ratio of the real and imaginary parts of the wave number for each case considered and consider the case in physical units where the emission is considered strong if significant energy is carried to distances $\gtrsim 10 R_E$. This is the case when $k_{x1r}/k_{x1i} \gtrsim 0.3$ for region 1 and $k_{x2r}/k_{x2i} \gtrsim 0.75$ for region 2. More significant wave emission, where waves can propagate to distances $\gtrsim 25 R_E$, is found to be possible for $k_{x2r,x1r}/k_{x2i,x1i} \gtrsim 1.0$. This shows that waves transition from being surface waves to propagating body waves. This generally happens when the phase velocity of the KHI waves reaches or exceeds background fast MHD wave phase speeds. Moreover, wave emission due to the effects of the KHI usually starts at the point where growth rates are decreasing with $k_y \Delta_x$.

We have investigated the effects of varying magnetic field direction in region 1, while the magnetic field direction in region 2 is kept constant. Four different θ_2 values were considered, while θ_1 was varied from $0 - \pi$.

For all of the θ_2 values considered we found that the growth rates peak at $\theta_1 = 90^\circ$, while modes supporting propagating wave emission was more probable for $\theta_1 \simeq 0-30^\circ$ and $\theta_1 \simeq 150-180^\circ$, which corresponds to the configurations where the magnetic field has a large component parallel or antiparallel to the boundary. These results also confirm that strong magnetic tension enhances MHD wave emission from a KH unstable boundary.

Applications of the results to shear flow boundaries in the Earth's magnetosphere and in the solar corona are discussed. We have concluded that on the boundaries of the dayside magnetopause and within interplanetary CMEs, KHI surface wave growth dominates the evolution of the boundary. In contrast, on the boundaries of the nightside magnetopause, magnetotail, BBF channels, SAD channels, coronal plumes, and coronal streamers, the shear flow may support the excitation of modes which emit propagating MHD wave disturbances from the boundary. This will also weaken the growth of the KH surface modes as a result of waves carrying energy away from shear flow boundaries of the flow channels. The generation of unstable KH modes which causes the emission of MHD waves can provide a significant source of energy transport between different regions. Moreover, KHI-driven wave emission and energy transport out of BBF and SAD channels may provide a possible explanation for the deceleration and stopping of BBFs and SADs.

Only perturbations along the background flow are considered in this study. Future studies include extending the analysis to perturbations propagating in arbitrary directions with respect to the background flow, which may significantly change the characteristics of fast magnetosonic wave emission due to the KHI.

Acknowledgments

I.R.M. and R.R. acknowledge financial support from the Canadian Space Agency (CSA) and the National Engineering and Research Council of Canada (NSERC). H.T. also benefited from financial support from NSERC and the CSA Space Science Enhancements Program. Interested readers may contact the author H.T. by e-mail turkakin@ualberta.ca for requesting data files to reproduce Figures 2–11.

References

- Andries, J., and M. Goossens (2001), Kelvin-Helmholtz instabilities and resonant flow instabilities for a coronal plume model with plasma pressure, *Astron. Astrophys.*, *368*, 1083–1094.
- Angelopoulos, V., W. Baumjohann, C. Kennel, F. Coroniti, M. Kivelson, R. Pellat, R. Walker, H. Lühr, and G. Paschmann (1992), Bursty bulk flows in the inner central plasma sheet, *J. Geophys. Res.*, *97*(A4), 4027–4039.
- Angelopoulos, V., et al. (1994), Statistical characteristics of bursty bulk flow events, *J. Geophys. Res.*, *99*(A11), 21,257–21,280.
- Angelopoulos, V., et al. (1997), Magnetotail flow bursts: Association to global magnetospheric circulation, relationship to ionospheric activity and direct evidence for localization, *Geophys. Res. Lett.*, *24*(18), 2271–2274.
- Baranov, V., H. J. Fahr, and M. S. Ruderman (1992), Investigation of macroscopic instabilities at the heliopause boundary surface, *Astron. Astrophys.*, *261*, 341–347.
- Cécere, M., E. Zurbriggen, A. Costa, and M. Scheneiter (2014), 3D MHD simulation of post-flare Supra-Arcade Downflows in a turbulent current sheet medium, *Astro-ph.SR*, *1*, 12.
- Chen, Y., H. Song, L. Li, Z. Xia, H. Wu, and L. Xing (2010), Streamer wave driven by coronal mass ejections, *Astrophys. J.*, *714*, 644–651.
- Contin, J. E., F. T. Gratton, and C. J. Farrugia (2003), Theoretical results on the latitude dependence of the Kelvin-Helmholtz instability at the day-side magnetopause of northward interplanetary magnetic field, *J. Geophys. Res.*, *108*(A6), 1227, doi:10.1029/2002JA009319.
- Fairfield, D. H., A. Otto, S. Kokobun, R. P. Lepping, J. T. Steinberg, A. J. Lazarus, and T. Yamamoto (2000), Geotail observation of Kelvin-Helmholtz instability at the equatorial magnetotail boundary for parallel northward fields, *J. Geophys. Res.*, *105*(A9), 21,159–21,173.
- Farrugia, C. J., F. Gratton, L. Bender, H. Biernat, N. Erkaev, J. Quinn, R. Torbert, and V. Dennisenko (1998), Chords of joint Kelvin-Helmholtz and Rayleigh-Taylor instabilities at the dayside magnetopause for strongly northward interplanetary magnetic field, *J. Geophys. Res.*, *103*(A4), 6703–6727.
- Feng, L., B. Inhester, and W. Gan (2013), Kelvin-Helmholtz instability of a coronal streamer, *Astrophys. J.*, *774*, 141–150, doi:10.1088/0004-637X/774/2/141.
- Foullon, C., C. J. Farrugia, A. N. Fazakerley, C. J. Owen, F. T. Gratton, and R. B. Torbert (2008), Evolution of Kelvin-Helmholtz activity on the dusk flank magnetopause, *J. Geophys. Res.*, *113*, A11203, doi:10.1029/2008JA013175.
- Foullon, C., C. J. Farrugia, C. J. Owen, A. N. Fazakerley, and F. R. Gratton (2010), Kelvin-Helmholtz multi-spacecraft studies at the Earth's magnetopause boundaries, *Twelfth Int. Solar Wind Conf.*, *1216*, 367–370, doi:10.1063/1.3395876.
- Foullon, C., E. Verwichte, V. Nakariakov, K. Nykyri, and C. Farrugia (2011), Magnetic Kelvin-Helmholtz instability at the Sun, *Astrophys. J. Lett.*, *729*, L8, doi:10.1088/20418205/729/1/L8.
- Foullon, C., E. Verwichte, K. Nykyri, J. Markus, and I. G. Hannah (2013), Kelvin-Helmholtz instability of the CME reconnection outflow layer in the solar corona, *Astrophys. J.*, *767*, 170, doi:10.1088/0004-637X/767/2/170.
- Gratton, F. T., G. Gnani, C. J. Farrugia, and L. Bender (2004), On the MHD boundary of Kelvin-Helmholtz stability diagram at large wavelengths, *Brazilian J. Phys.*, *34*(4B), 1804–1813.
- Grigorenko, E. E., R. Koleva, and J.-A. Sauvaud (2012), On the problem of plasma sheet boundary layer identification from plasma moments in Earth's magnetotail, *Ann. Geophys.*, *30*, 1331–1343, doi:10.5194/angeo-30-1331-2012.
- Hasegawa, H., M. Fujitomo, K. Takagi, Y. Saito, and H. Réme (2006), Single-spacecraft detection of rolled-up Kelvin-Helmholtz vortices at the flank magnetopause, *J. Geophys. Res.*, *111*, A09203, doi:10.1029/2006JA011728.
- Hwang, K.-J., M. M. Kuznetsova, F. Sahraoui, M. L. Goldstein, E. Lee, and G. K. Parks (2011), Kelvin-Helmholtz waves under southward IMF, *J. Geophys. Res.*, *116*, A08210, doi:10.1029/2011JA016596.
- Jean, R., and J. Laurent (2000), The baroclinic secondary instability of the two-dimensional shear layer, *Phys. Fluids*, *12*(10), 2489–2505.
- Lai, S. H., and L. H. Lyu (2006), Nonlinear evolution of MHD Kelvin-Helmholtz instability in a compressible plasma, *J. Geophys. Res.*, *111*, A01202, doi:10.1029/2004JA010724.
- Lai, S. H., and L. H. Lyu (2008), Nonlinear evolution of jet-flow-associated Kelvin-Helmholtz instability in MHD plasmas and the formation of Mach-cone-like plane waves, *J. Geophys. Res.*, *113*, A06217, doi:10.1029/2007JA012790.
- Landau, L. D., and E. M. Lifshitz (1987), *Fluid Mechanics*, 259–262 pp., Pergamon Press, Oxford.
- Lawrence, G. A., F. K. Browand, and L. G. Redekopp (1991), The stability of a sheared density interface, *Phys. Fluids*, *3*, 2360–2370.

- Liu, W., and L. Ofman (2006), Advances in observing various coronal EUV waves in the SDO era and their seismological applications, *Sol. Phys.*, *289*(9), 3233–3277, doi:10.1007/s11207-014-0528-4.
- Ma, Y., C. Shen, V. Angelopoulos, A. T. Y. Lui, X. Li, H. U. Frey, M. Dunlop, H. U. Auster, J. P. McFadden, and D. Larson (2012), Tailward leap of multiple expansion of plasmashet during a moderately intense substorm: THEMIS observation, *J. Geophys. Res.*, *117*, A07219, doi:10.1029/2012JA017768.
- Malik, M. R., F. Li, and C.-L. Chang (1994), Cross-flow disturbances in three-dimensional boundary layers: Nonlinear development, wave interaction and secondary instability, *J. Fluid Mech.*, *268*, 1–36.
- Mann, I. R., A. N. Wright, K. J. Mills, and V. M. Nakariakov (1999), Excitation of magnetospheric waveguide modes by magnetosheath flows, *J. Geophys. Res.*, *104*(A1), 333–353.
- McKenzie, D. E., and S. Savage (2009), Quantitative examination of Supra-Arcade Downflows in eruptive solar flares, *Astrophys. J.*, *697*, 1569–1577.
- McPherron, R. L., T.-S. Hsu, J. Kissinger, X. Chu, and V. Angelopoulos (2011), Characteristics of plasma flows at the inner edge of the plasma sheet, *J. Geophys. Res.*, *116*, A00133, doi:10.1029/2010JA015923.
- Miura, A. (1982), Nonlinear evolutions of the magnetohydrodynamic Kelvin-Helmholtz instability, *Plasma Rev. Lett.*, *49*(11), 779.
- Miura, A., and P. L. Pritchett (1982), Nonlocal stability analysis of the MHD Kelvin-Helmholtz instability in a compressible plasma, *J. Geophys. Res.*, *87*(A9), 7431–7444.
- Möstl, U., M. Temmer, and M. Veronic (2013), The Kelvin-Helmholtz instability at coronal mass ejection boundaries in the solar corona: Observations and 2.5D MHD simulations, *Astrophys. J. Lett.*, *776*(L12), doi:10.1088/2041-8205/766/1/L12.
- Nakai, H., and G. Ueno (2011), Plasma structures of Kelvin-Helmholtz billows at the dusk-side flank of the magnetotail, *J. Geophys. Res.*, *116*, A08212, doi:10.1029/2010JA0116286.
- Nykyri, K., and C. Foullon (2013), First magnetic seismology of the CME reconnection outflow layer in the low corona with 2.5D MHD simulations of Kelvin-Helmholtz instability, *Geophys. Res. Lett.*, *40*, 4154–4159, doi:10.1002/grl.50807.
- Ofman, L., and B. Thompson (2011), SDO/AIA observation of Kelvin-Helmholtz instability in the solar corona, *Astrophys. J. Lett.*, *734*, L11.
- Ong, R. S. B., and N. Roderick (1972), On the Kelvin-Helmholtz instability of the Earth's magnetopause, *Planet. Space Sci.*, *20*, 1–10.
- Press, W., S. A. Teukolsky, W. T. Vetterling, and B. P. Flannery (2002), *Numerical Recipes in C++*, 784–785 pp., Cambridge Univ. Press, Cambridge, U. K.
- Pu, Z.-Y., and M. G. Kivelson (1983), Kelvin-Helmholtz instability at the magnetopause: Solution for compressible plasmas, *J. Geophys. Res.*, *88*(A2), 841–852.
- Rankin, R., P. Frycz, and J. Samson (1997), Shear flow vortices in magnetospheric plasmas, *Phys. Plasmas*, *4*, 829–840.
- Ruderman, M. S., and H. Fahr (1995), The effect of magnetic fields on the macroscopic instability of the heliopause—2. Inclusion of solar wind magnetic fields, *Astron. Astrophys.*, *299*, 258–266.
- Sergeev, V., A. Runov, W. Baumjohann, R. Nakamura, T. Zhang, A. Balogh, P. Louarn, J. A. Sauvaud, and H. Rème (2004), Orientation and propagation of current sheet oscillations, *Geophys. Res. Lett.*, *31*, L05807, doi:10.1029/2003GL019346.
- Shiokawa, K., W. Baumjohann, and G. Haerendel (1997), Braking of high-speed flows in the near-Earth tail, *Geophys. Res. Lett.*, *24*(10), 1179–1182.
- Southwood, D. J. (1974), Some features of field line resonances in the magnetosphere, *Planet. Space Sci.*, *22*, 483–491.
- Takagi, K., C. Hashimoto, H. Hasegawa, M. Fujitomo, and R. TanDokoro (2006), Kelvin-Helmholtz instability in a magnetotail flank-like geometry: Three-dimensional MHD simulations, *J. Geophys. Res.*, *111*, A08202, doi:10.1029/2006JA011631.
- Taroyan, Y., and R. Erdélyi (2002), Resonant and Kelvin-Helmholtz instabilities on the magnetopause, *Phys. Plasmas*, *9*(7), 3121–3129.
- Taroyan, Y., and R. Erdélyi (2003), Resonant surface waves and instabilities in finite β plasmas, *Phys. Plasmas*, *10*(1), 266–276.
- Taroyan, Y., and M. Ruderman (2011), MHD waves and instabilities in space plasma flows, *Space Sci. Rev.*, *158*, 505–523, doi:10.1007/s11214-010-9737-9.
- Turkakin, H., R. Rankin, and I. R. Mann (2013), Primary and secondary compressible Kelvin-Helmholtz surface waves instabilities on the Earth's magnetopause, *J. Geophys. Res. Atmos.*, *118*, doi:10.1002/jgra.50394.
- Turkakin, H., I. R. Mann, and R. Rankin (2014), Kelvin-Helmholtz unstable magnetotail flow channels: Deceleration and radiation of MHD waves, *Geophys. Res. Lett.*, *41*, 3691–3697, doi:10.1002/2014GL060450.
- Volwerk, M., et al. (2005), Plasma flow channels with ULF waves observed by Cluster and Double Star, *Ann. Geophys.*, *23*, 2929–2935.
- Volwerk, M., K.-H. Glassmeier, R. Nakamura, T. Takada, W. Baumjohann, B. Klecker, H. Rème, T. Zhang, E. Lucek, and C. Carr (2007), Flow burst-induced Kelvin-Helmholtz waves in the terrestrial magnetotail, *Geophys. Res. Lett.*, *34*, L10102, doi:10.1029/2007GL029459.
- Walker, A. D. M. (1981), Kelvin-Helmholtz instability in the low-latitude boundary layer, *Planet. Space Sci.*, *29*(10), 1119–1133.
- Zhang, T., et al. (2005), Double Star/Cluster observation of neutral sheet oscillations on 5 August 2004, *Ann. Geophys.*, *23*, 2909–2914.